Ternary chalcogenides NbInX2 (X = S, Se): A comprehensive investigation of mechanical, electronic, vibrational, optical and thermophysical properties

Article *in* International Journal of Modern Physics B · December 2024

DOI: 10.1142/S0217979225501188

CITATIONS
2

READS
251

4 authors:

Md. Hasan Mia
International Islamic University Chittagong
9 PUBLICATIONS **12** CITATIONS
SEE PROFILE

Fahmida Parvin
University of Rajshahi
76 PUBLICATIONS **1,064** CITATIONS
SEE PROFILE

A. K. M. A. Islam
International Islamic University Chittagong
309 PUBLICATIONS **4,998** CITATIONS
SEE PROFILE

Mst. Asma Khatun
Hajee Mohammad Danesh Science and Technology University
8 PUBLICATIONS **8** CITATIONS
SEE PROFILE

International Journal of Modern Physics B
(2025) 2550118 (31 pages)

DOI: 10.1142/S0217979225501188

World Scientific
www.worldscientific.com

Ternary chalcogenides $NbInX_2$ (X = S, Se): A comprehensive investigation of mechanical, electronic, vibrational, optical and thermophysical properties

M. H. Mia [*,‡], F. Parvin [*,¶], A. K. M. A. Islam [*,†] and Mst. A. Khatun [*,§]

[*]*Department of Physics, University of Rajshahi*
Rajshahi 6205, Bangladesh

[†]*Department of EEE*
International Islamic University Chittagong, Kumira
Chittagong 4318, Bangladesh

[‡]*Department of Textile Engineering, Uttara University*
Uttara-16, Dhaka 1230, Bangladesh

[§]*Department of Physics*
Hajee Mohammad Danesh Science and Technology University
Dinajpur 5200, Bangladesh
[¶]*fparvin@ru.ac.bd*

Received 16 October 2023
Revised 11 August 2024
Accepted 2 October 2024
Published 26 December 2024

A comprehensive investigation of the unexplored mechanical, electronic, Mulliken bond population, vibrational, optical and thermophysical properties of the synthesized compounds $NbInX_2$ (X = S, Se) have been made for the first time using the density functional theory. The chemical, mechanical and dynamical stabilities of the compounds are established in our calculations. Both compounds are soft, machinable and brittle. The anisotropic nature of the studied compounds is shown by 3D representations of elastic moduli. The density of states and electronic band structure demonstrate that the compounds are metallic. Fermi surfaces of both compounds are almost similar and contain both hole- and electron-like topologies. The characteristics of chemical bonding among different atoms of the compounds are studied via a charge density distribution map and bond population analysis. Both the compounds possess optical anisotropy. Reflectivity is high (above 44%) in the IR–visible–UV region indicating that the phases may be effective in reducing solar heat. Minimum thermal conductivity, k_{min} (used to select appropriate material for thermal barrier coating) and its anisotropy are calculated for the first time. The results show that both compounds have k_{min} much smaller than the reference value of 1.25 $W\,m^{-1}\,K^{-1}$.

Keywords: Density functional theory; electronic property; mechanical property; thermophysical property; Fermi surface; minimum thermal conductivity.

PACS numbers: 71.15.Mb, 72.15.–v, 68.60.Bs, 65.40.–b, 71.18.+y

[¶]Corresponding author.

1. Introduction

The compounds that contain at least one chalcogen element such as sulfur, selenium, tellurium and are called chalcogenides. These materials have recently received much attention from the scientific community because of their interesting physical properties and potential use in devices such as logic transistors, field-effect transistors (FETs), photodetectors, and photoelectrochemical cells. These are also promising candidates for optoelectronic device applications because of their various crystalline phases and fascinating properties associated with thermoelectric effects. Although most chalcogenides are semiconductors, our studied compounds $NbInS_2$ and $NbInSe_2$ show metallic character. $NbInS_2$ and $NbInSe_2$ ternary chalcogenides are prepared by intercalating the post-transition element In with the dichalcogenides NbS_2 and $NbSe_2$. By using X-ray powder methods, Eppinga *et al.*[1] synthesized M_xNbX_2 and M_xTaX_2 ($M =$ In, Sn, Pb, Bi; $X =$ S, Se) in 1980. They reported the experimental lattice parameters of $InNbS_2$ and In_xNbSe_2 $(2/3 \leq x \leq 1)$ along with other compounds. In 1982, Sunandana *et al.*[2] also synthesized $In_{0.67}NbS_2$ and $In_{0.67}NbSe_2$ accompanied by other compounds using powder X-ray diffraction method. They studied the electrical characteristics of $In_x MCh_2$ ($M =$ Nb, Ta; $Ch =$ S, Se) and found that all the compounds show metallic behavior.

In 2012, Zhang *et al.*[3] synthesized $NaInS_2$ by solvothermal method doped with Cu. According to their findings, Cu doping causes photocatalytic enhancements in the presence of visible light. Yaseen *et al.*[4] and Hossain *et al.*[5] theoretically reported optoelectronic and thermoelectric properties of $NaInS_2$ and $NaInSe_2$. They show that $NaInS_2$ and $NaInSe_2$ are narrow band gap semiconductors. In the ultraviolet range, these compounds exhibit high optical absorption and low reflectance, making them excellent for optoelectronic applications.

In 2013, Wu *et al.*[6] also synthesized $CuInS_2$ ternary compound using a solvothermal procedure based on CuS microspheres as sacrificial templates. They claimed that $CuInS_2$ has substantial infrared optical absorption and is a promising agent for polythermal conversion. In 2020, Soni *et al.*[7] theoretically studied the electronic and optical properties of $CuInS_2$ and $CuGaS_2$ chalcopyrites. In 2008, Wang *et al.*[8] synthesized $CuInS_2$ and $AgInS_2$ by powder X-ray diffraction (XRD) and obtained metastable orthorhombic phase of $AgInS_2$, $CuInS_2$ and $AgInSe_2$. In 2020, Yuan *et al.*[9] also synthesized $AgInS_2$ by one-step hydrothermal method and reported that the optical band gap increases with molar ratio of Ag–In–S. The photoelectric and photocatalytic properties of $AgInS_2$ were also studied at 200°C temperatures.

To the best of our knowledge, elastic, electronic (such as electronic spectra, density of states, Fermi surface, electronic charge density distribution), thermophysical, optical and vibrational properties of $NbInS_2$ and $NbInSe_2$ have not yet been studied theoretically and experimentally. All the above-mentioned properties are important for technological applications. Mechanical characteristics inform us about the practical usage of materials. Elastic constants are required for a variety of practical applications involving a solid's mechanical characteristics. The band

structure helps one to predict the electronic properties of a compound. The optical characteristics of a substance reveal the material's reaction to incoming radiation. So, the frequency-dependent optical constants such as dielectric constants, absorptivity, reflectivity, refractivity, loss function and optical conductivity are essential for optoelectronic applications. Hence, the theoretical investigation on the above-mentioned properties of $NbInX_2$ (X = S, Se) are required in order to fully exploit their features for eventual technological applications.

Here, we have studied the aforementioned properties along with different thermophysical properties such as Debye temperature, melting temperature, Grüneisen parameter, heat capacity, thermal expansion coefficient, and minimum thermal conductivity in detail. The main objective of our study is to fill up this essential research gap of chalcogenide phases in detail, which can be immensely helpful for future research when viewed from an applied and basic research point of view.

The rest of the paper is structured as follows. An explanation of the computational methodology is included in Sec. 2. In Sec. 3, the new findings are analyzed and presented. Finally, Sec. 4 summarizes the results.

2. Computational Method

First-principles calculations are performed within the context of density functional theory[10] utilizing the plane wave pseudopotential technique implemented in the Cambridge Serial total Energy Package (CASTEP) code.[11] For different atoms, plane wave pseudopotentials replace the complex potential felt by core electrons with a simpler and smooth potential. This allows for efficient calculations without directly solving for core electrons. The core–valence separation is designed such that core electrons are not explicitly included in the calculations but their effects are approximated by the pseudopotential. The interaction between valence electrons and ionic core is estimated using Vanderbilt-type ultrasoft pseudopotentials.[12] The local density approximation (LDA) CA-PZ (introduced by Ceperley and Alder; parametrized by Perdew and Zunger)[13–15] is used to perform the exchange-correlation energy term when solving the Kohn–Sham equations. The ground state energy of $NbInX_2$ (X = S, Se) is investigated using the Broyden–Fletcher–Goldfrab–Shanno (BFGS) optimization technique.[16] The values of kinetic energy cut-off for the plane wave expansion are taken as 650 and 500 eV for $NbInS_2$ and $NbInSe_2$, respectively. Kinetic energy cut-off is a crucial parameter which has enormous effect on the quality of the DFT calculations. It tells us about the cutoff of the number of plane wave functions being utilized as basis functions to represent the wavefunction. According to the Monkhorst–Pack method,[17] integration over the first Brillouin zone is performed using $22 \times 22 \times 8$ k-point mesh for both tompounds. This dense k-point mesh yields smoother electronic spectra, Fermi topology and electronic charge density map. Geometry optimization is performed using threshold values of 5×10^{-6} eV/atom for the total energy, 0.01 eV/Å for the maximum force, 0.02 GPa for the maximum stress and 5×10^{-4} Å for maximum displacement. Using the finite

stress–strain method[18] based on DFT, the elastic and mechanical properties have been calculated. The anisotropic nature of elastic characteristics is demonstrated by ELATE software.[19]

3. Results and Analysis

3.1. *Structural properties and chemical stability*

The ternary compounds $NbInX_2$ (X = S, Se) are hexagonal crystals having space group $P\bar{6}m2$ (No. 187). The optimized crystal structure is shown in Fig. 1. The unit cell consists of one formula unit with a total of four atoms. The positions of Nb, In, X atoms are at $1b(0, 0, 1/2)$, $1a(0, 0, 0)$ and $2i(1/3, 2/3, z_x)$ Wyckoff sites, respectively, where z_x is the internal parameter (Table 1). The optimized parameters for $NbInX_2$ (X = S, Se) are shown in Table 1 along with available experimental[1] data for comparison. It is observed that our calculated lattice parameters reasonably agree with these and hence our present study is credible.

Although our studied compounds are experimentally synthesized, the cohesive energy of the studied compounds has been determined to verify their chemical stability. The chemical stability of the structure of solids can be measured directly

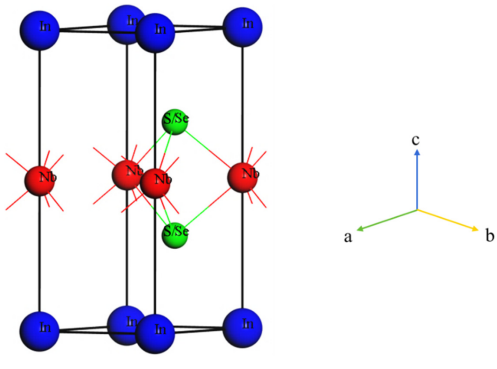

Fig. 1. (Color online) The optimized unit cell of $NbInX_2$ (X = S, Se). On the right, the crystallographic axes are displayed.

Table 1. Lattice parameters a and c (Å), c/a ratio, internal parameter z_X (X = S, Se), unit cell volume V (Å^3) and cohesive energy E_{coh} (eV/atom) for $NbInS_2$ and $NbInSe_2$.

Compound	a	C	c/a	z_X	V	E_{coh}	Ref.
$NbInS_2$	3.302	7.949	2.407	0.31	75.07	1.71	This work
	3.340	8.160	2.443	0.32	78.83	—	Expt.[1]
$NbInSe_2$	3.419	8.245	2.412	0.30	83.49	0.40	This work
	3.450	9.270	2.687	0.32	95.55	—	Expt.[1,†]
$NbIn_{0.67}Se_2$	3.410	9.260	2.715	—	93.25	—	Expt.[2]

Note: †Quoted values for In_xNbSe_2 ($2/3 \leq x \leq 1$).

from the difference between crystal energy and free atom energy of the relevant phases. The cohesive energy per atom is calculated using the following equation[18,20]:

$$E_{\text{coh}} = \frac{(E_{\text{Nb}} + E_{\text{In}} + 2E_X - E_{\text{NbIn}X_2})}{4}, \tag{1}$$

where $E_{\text{NbIn}X_2}$ is total crystal energy per formula unit of $\text{NbIn}X_2$ and E_{Nb}, E_{In} and E_X are total energies of single Nb, In and X atoms, respectively. CASTEP code is used to calculate the isolated atomic energies. Our estimated values of E_{coh} are listed in Table 1. The positive values of cohesive energies indicate that these materials are chemically stable.

3.2. *Elastic and mechanical properties*

3.2.1. *Elastic properties*

The elastic constants provide a relationship between the mechanical and dynamic behavior of crystals.[21] We have estimated the independent single crystal elastic constants C_{ij}, polycrystalline bulk (B_V, B_R and B_H) and shear moduli (G_V, G_R and G_H), Young's modulus Y and Poisson's ratio ν of the ternary chalcogenides $\text{NbIn}X_2$ ($X = \text{S, Se}$) for the first time. Further information on elastic constants may be found elsewhere.[22–24] For hexagonal crystals,[23] the number of components of the tensor of elastic constants decreases to five: C_{11}, C_{33}, C_{44}, C_{12} and C_{13}. We are unable to compare our estimated elastic constants with any other theoretical or experimental data, unfortunately.

For a hexagonal system, the elastic constants must meet the following stability criteria[24,25] (at zero pressure) in order to be mechanically stable:

$$\begin{gathered} C_{11} - |C_{12}| > 0, \\ (C_{11} + C_{12})C_{33} - 2C_{13}^2 > 0, \\ C_{44} > 0. \end{gathered} \tag{2}$$

Our estimated elastic constants are presented in Table 2, which fulfill the aforementioned stability requirements. These suggest that $NbInS_2$ and $NbInSe_2$ are mechanically stable.

We know C_{11} and C_{33} represent the axial resistances along a- and c-axes, respectively. Table 2 shows that our estimated values of C_{11} and C_{33} are larger than other elastic constants, which indicates that the titled compounds are more incompressible under uniaxial stress along a (ϵ_{11}) or c (ϵ_{33}) axis. For both $NbInS_2$ and

Table 2. Single crystal elastic constants C_{ij} (GPa), linear compressibility ratio k_c/k_a, Kleinman parameter (ζ) and tetragonal shear modulus C_t (GPa) for $NbInS_2$ and $NbInSe_2$.

Compound	C_{11}	C_{33}	C_{44}	C_{12}	C_{13}	k_c/k_a	ζ	C_t
$NbInS_2$	144.5	116.7	47.9	40.3	42.7	1.34	0.43	52.10
$NbInSe_2$	177.1	172.3	60.7	55.9	64.0	0.97	0.46	60.59

$NbInSe_2$, C_{11} is higher than C_{33} indicating that c-axis is more compressible than a-axis. C_{44} is a crucial parameter pertaining to the shear modulus, which represents the resistance to shear deformation of the crystal. As both compounds have lower values of C_{44} than those of C_{11} and C_{33}, shear deformation may occur more readily than uniaxial stresses. Moreover, the other two elastic constants C_{12} and C_{13} are referred to as the off-diagonal shear components.

For hexagonal crystal structure, the linear compressibility coefficient ratio along the a- and c-axes is calculated using the following relation[26]:

$$\frac{k_c}{k_a} = \frac{C_{11} + C_{12} - C_{13}}{C_{33} - C_{13}}, \tag{3}$$

where k_c and k_a denote the compressibility along the c- and a-directions, respectively. Our estimated k_c/k_a indicates that $NbInS_2$ has greater compressibility along c-axis compared to $NbInSe_2$.

The Kleinman parameter (ζ), commonly known as the internal strain parameter, assesses the stability of a material to stretching or bending. The ζ can be calculated using the following expression[27]:

$$\zeta = \frac{C_{11} + 8C_{12}}{7C_{11} + 2C_{12}}. \tag{4}$$

ζ is a dimensionless parameter with a value that is typically in the range of $0 \leq \zeta \leq 1$. The maximum limit of ζ is 1, which indicates bond bending, on the other hand, the lower limit of ζ is 0, which indicates bond stretching.[28] The estimated values of $NbInS_2$ and $NbInSe_2$ are 0.43 and 0.46, respectively, and are shown in Table 2. These suggest that the mechanical strength in both $NbInS_2$ and $NbInSe_2$ is mostly dominated by the contribution of bond stretching as opposed to bond bending.

The tetragonal shear modulus C_t can be calculated as[29] $C_t = \frac{C_{11}-C_{12}}{2}$. The sound velocity (transverse waves) in a material and its dynamical stability are intimately related to this characteristic parameter.[29] Large positive values of C_t indicate that our studied compounds are dynamically stable.

3.2.2. *Mechanical properties*

Using the Voigt–Reuss–Hill (VRH) approximation, the mechanical properties of a material are determined by its bulk, shear, Young's moduli (B_H, G_H, Y) and Poisson's ratio ν, which have been evaluated by the following relations[30–32]:

$$\left.\begin{aligned} B_V &= (2C_{11} + 2C_{12} + C_{33} + 4C_{13})/9 \quad \text{and} \\ B_R &= C^2/M \end{aligned}\right\}, \tag{5}$$

$$\left.\begin{aligned} G_V &= (M + 3C_{11} - 3C_{12} + 12C_{44} + 6C_{66})/30 \quad \text{and} \\ G_R &= 15\Big/\left[\frac{18B_V}{C^2} + \frac{6}{(C_{11} - C_{12})} + \frac{6}{C_{44}} + \frac{3}{C_{66}}\right] \end{aligned}\right\}, \tag{6}$$

where $M = C_{11} + C_{12} + 2C_{33} - 4C_{13}$ and $C^2 = (C_{11} + C_{12})C_{33} - 2C_{13}^2$.

The average values of B and G, denoted by B_H and G_H, respectively, were then determined using the following Hill averaging approach[32]:

$$\left.\begin{aligned} B = B_H = (B_R + B_v)/2 \quad \text{and} \\ G = G_H = (G_R + G_v)/2 \end{aligned}\right\}. \tag{7}$$

Young's modulus (Y) and Poisson's ratio (ν) were subsequently obtained from the calculated bulk and shear moduli using the following expression[32]:

$$\left.\begin{aligned} Y = \frac{9GB}{3B+G} \quad \text{and} \\ \nu = \frac{3B-2G}{2(3B+G)} \end{aligned}\right\}. \tag{8}$$

The bulk modulus B assesses the resistance of a material to volume deformation. On the other hand, the shear modulus G uniformly anticipates the strength to increase the shape-change resistance or plastic deformation. Table 3 shows that our estimated values of B and G are much smaller than that of super hard materials t-B_4CO_4 ($B = 250$ GPa, $G = 220$ GPa)[33] and t-NB_2 ($B = 298$ GPa, $G = 295$ GPa).[34] The low values of B and G indicate that our studied compounds are soft and easily machinable. The Vickers hardness of these compounds are also expected to be low. Young's modulus, Y, is a way to measure the stiffness of a material; the higher the value of Y, the stiffer the material. Despite the fact that the Y values of our investigated compounds are lower than those of hard materials, it can be inferred from a comparison of our estimated Y values that $NbInSe_2$ is stiffer than $NbInS_2$. Again, Y is inversely proportional to the thermal shock resistance, R.[35] Hence $NbInS_2$ possesses large thermal shock resistance compared to $NbInSe_2$.

Poisson's ratio, v, is a characteristic feature of crystalline solids that facilitates the computation of several physical parameters of crystalline solids, including prediction of the stability under shear,[36] which is obtained by the low value of ν. In addition, it estimates the nature of the interatomic forces of solids.[37,38] The central forces among constituents in solids are characterized by the value of ν within the range from 0.25 to 0.50, and if v is outside of this range, a crystalline system is considered to have non-central forces.[39] In this study, ν is estimated using bulk and shear moduli of the compounds. In the case of $NbInS_2$ and $NbInSe_2$, the ν values are 0.23 and 0.25, which imply that the interatomic forces in $NbInS_2$ are predominantly noncentral but in $NbInSe_2$ are central-force. The chemical bonding in crystals is explored by Poisson's ratio.[40] For a perfect covalent, ionic and metallic material, the Poisson's ratio is 0.1, 0.25 and 0.33,

Table 3. Bulk modulus, B (GPa) and shear modulus, G (GPa) (by VRH method), Young's modulus, Y (GPa), Poisson's ratio, ν, Pugh's ratio and machinability index, μ_M of $NbInS_2$ and $NbInSe_2$.

Compounds	B_R	B_V	B_H	G_R	G_V	G_H	Y	ν	G/B	μ_M
$NbInS_2$	72.4	73.0	72.7	47.8	48.2	48.0	118.0	0.23	0.66	1.52
$NbInSe_2$	99.4	99.4	99.4	59.2	59.2	59.2	148.1	0.25	0.60	1.64

respectively. Hence, the ionic bonding mainly contributes to the chemical bonds of $NbInX_2$ (X = S, Se). According to Frantsevich's rule,[41] a material having $\nu < 0.26$ behaves in a brittle manner; otherwise, ductile. Our estimated values of ν (Table 3) for $NbInS_2$ and $NbInSe_2$ suggest that both compounds are brittle in nature.

Again, in Pugh's ratio $G/B < 0.57$,[42] a substance exhibits malleable behavior, else it is fragile. Our estimated G/B ratio of $NbInX_2$ (X = S, Se) are 0.66 and 0.60, respectively, which also indicate the brittleness of titled compounds.

The machinability index, μ_m is used to check the machinability of a crystalline material. The machinability index provides important information on the surface of a material's integrity, tool life, cutting stresses and demand for power. The machinability index is given by the following equation[43]:

$$\mu_m = \frac{B}{C_{44}}. \tag{9}$$

Moreover, the ratio B/C_{44} can be used to determine plasticity.[44–46] It also measures the lubricity of bulk materials. Lower C_{44} values of both compounds are found to make these machinable. Our estimated values of μ_m (shown in Table 3) indicate that these compounds have the potential to be used as dry lubricants.

3.3. *Anisotropy index of elasticity*

Elastic anisotropy is often used to identify microcracks in material. Due to the association between the anisotropic behavior and the potential for microcracks inside crystals under different stress, knowledge about this parameter is important in engineering as well as crystal physics. The shear anisotropic factors A_1, A_2 and A_3 provide different types of bonding in different directions. Details on these parameters can be found elsewhere.[36,47] For a hexagonal crystal, the factors A_1, A_2 and A_3 are expressed as follows[36,47]:

$$A_1 = \frac{4C_{44}}{C_{11} + C_{33} - 2C_{13}}, \tag{10}$$

$$A_2 = \frac{4C_{55}}{C_{22} + C_{33} - 2C_{23}}, \tag{11}$$

$$A_3 = \frac{4C_{66}}{C_{11} + C_{22} - 2C_{12}}. \tag{12}$$

The value of A should be one for a perfectly isotropic crystal, whereas smaller or larger than one refers to the crystal's degree of elastic anisotropy.[48] It is evident from Table 4 that $NbInS_2$ and $NbInSe_2$ are anisotropic in nature according to the shear anisotropy factors (A_1 and A_2) but the degree of anisotropy is very small for $NbInSe_2$. It is observed that A_3 is 1, which is interesting.

The universal log-Euclidean index is defined by the following equation[49,50]:

$$A^L = \sqrt{\left[\ln\left(\frac{B^V}{B^R}\right)\right]^2 + 5\left[\ln\left(\frac{C_{44}^V}{C_{44}^R}\right)\right]^2}. \tag{13}$$

Table 4. The universal anisotropy index A^U, anisotropy in compressibility and shear (A^B, A^G), Zener anisotropy A^{eq}, shear anisotropy indices (A_1, A_2 and A_3) and universal log-Euclidean index A^L for $NbInS_2$ and $NbInSe_2$.

Species	A^U	A^B	A^G	A^{eq}	A_1	A_2	A_3	A^L
$NbInS_2$	0.050	0.004	0.004	1.23	1.090	1.090	1	0.01
$NbInSe_2$	0.000	0.000	0.000	1.00	1.098	1.098	1	0.00

where C_{44}^V and C_{44}^R are obtained from[49]

$$C_{44}^R = \frac{5}{3}\left\{\frac{C_{44}(C_{11}-C_{12})}{3(C_{11}-C_{12})+4C_{44}}\right\} \tag{14}$$

and

$$C_{44}^V = C_{44}^R + \frac{3}{5}\left\{\frac{(C_{11}-C_{12}-2C_{44})^2}{3(C_{11}-C_{12})+4C_{44}}\right\}. \tag{15}$$

Similar to the universal anisotropy index A^U, A^L can be applied to all crystal symmetries. Strongly anisotropic or nearly isotropic materials are particularly interesting to evaluate. A^L values range from 0 to 10.26. Approximately 90% of crystalline solids have an A^L value below 1, whereas $A^L = 0$ for fully isotropic crystal.

The universal anisotropy factor A^U, anisotropy in compressibility and shear A^B, A^G, and equivalent Zener anisotropy A^{eq} are calculated using the frequently used relations shown below[49,51,52]:

$$A^U = \frac{B_V}{B_R} + 5\frac{G_V}{G_R} - 6 \geq 0, \tag{16}$$

$$A^B = \frac{B_V - B_R}{B_V + B_R}, \tag{17}$$

$$A^G = \frac{G_V - G_R}{G_V + G_R}, \tag{18}$$

$$A^{eq} = \left(1 + \frac{5}{12}A^U\right) + \sqrt{\left(1 + \frac{5}{12}A^U\right)^2 - 1}. \tag{19}$$

Ranganathan and Ostoja-Starzewski[52] defined A^U to assess anisotropy without taking into account crystal symmetry. $A^U = 0$ for elastically isotropic crystals while $A^U > 0$ signifies anisotropy. Again, for A^G and A^B, the maximum anisotropy is represented by a value of 1, while zero denotes elastic isotropy. According to the estimated values of A^U, A^G, A^B and A^L, $NbInS_2$ is slightly anisotropic. On the other hand, $NbInSe_2$ shows isotropic nature due to its equal B_V, B_R, G_V, G_R and C_{44}^V, C_{44}^R values. A value of one for equivalent Zener anisotropy, A^{eq} indicates isotropy for a crystalline material, whereas any other value denotes anisotropy.

It is simple to calculate B of a material in different crystallographic directions using pressure-dependent lattice constants. The uniaxial bulk modulus and anisotropies of the bulk modulus along the a-, b-, and c-axes can be represented as follows[28]:

$$B_a = a\frac{dP}{da} = \frac{\Lambda}{1+\alpha+\beta}, \tag{20}$$

$$B_b = b\frac{dP}{db} = \frac{B_a}{\alpha}, \tag{21}$$

$$B_c = c\frac{dP}{dc} = \frac{B_a}{\beta}, \tag{22}$$

$$B_{\text{relax}} = \frac{\Lambda}{(1+\alpha+\beta)^2}, \tag{23}$$

where

$$\Lambda = C_{11} + 2C_{12}\alpha + C_{22}\alpha^2 + 2C_{13}\beta + C_{33}\beta^2 + 2C_{33}\alpha\beta, \tag{24}$$

$$\alpha = \frac{\{(C_{11}-C_{12})(C_{33}-C_{13})\} - \{(C_{23}-C_{13})(C_{11}-C_{13})\}}{\{(C_{33}-C_{13})(C_{22}-C_{12})\} - \{(C_{13}-C_{23})(C_{12}-C_{23})\}}, \tag{25}$$

$$\beta = \frac{\{(C_{22}-C_{12})(C_{11}-C_{13})\} - \{(C_{11}-C_{12})(C_{23}-C_{12})\}}{\{(C_{22}-C_{12})(C_{33}-C_{13})\} - \{(C_{12}-C_{23})(C_{13}-C_{23})\}}. \tag{26}$$

The estimated values of B_a, B_b and B_c are displayed in Table 5. As the studied compounds are hexagonal, we found $B_a = B_b$. Table 5 demonstrates that $NbInS_2$ is more squeezable along the c-axis than a- or b-axis when pressure is applied, and vice versa for $NbInSe_2$. α and β represent the relative change in the b- and c-axes with the distortion of a-axis.

The relaxed bulk modulus, B_{relax}, is a characteristic property of a material that can be used to describe the stress relaxation of materials. The value of B_{relax} of $NbInS_2$ and $NbInSe_2$ are listed in Table 5. It is notable from this table that for both compounds our estimated relaxed bulk modulus, B_{relax}, is slightly deviated from the calculated bulk modulus (Table 3). It is used to characterize the thermal transition behavior of viscoelastic and polymer materials under constant strain.

A_{B_a} and A_{B_c} are the bulk modulus anisotropies along the crystallographic axes a and c with respect to b-axis and expressed as[28]

$$A_{B_a} = \frac{B_a}{B_b} = \alpha, \tag{27}$$

$$A_{B_c} = \frac{B_c}{B_b} = \frac{\alpha}{\beta}. \tag{28}$$

Table 5. Uniaxial bulk moduli B_a, B_b, B_c (GPa), α, β, relaxed bulk modulus B_{relax} (GPa), A_{B_a} and A_{B_c} for the compounds $NbInS_2$ and $NbInSe_2$.

Species	B_a	B_b	B_c	α	β	B_{relax}	A_{B_a}	A_{B_c}
$NbInS_2$	233.39	233.39	173.75	1	1.34	69.81	1	0.74
$NbInSe_2$	296.27	296.27	305.88	1	0.97	99.80	1	1.03

In Table 5, the calculated values of A_{B_a} and A_{B_c} are also listed. For these parameters, the value of 1 indicates elastic isotropy while any deviation from 1 measure a degree of elastic anisotropy possessed by the crystal. These values imply anisotropy in axial bulk modulus for both $NbInS_2$ and $NbInSe_2$.

We have also studied the directional-dependent anisotropy in Young's and shear moduli, linear compressibility and Poisson's ratio using ELATE[19] code. The directional-dependent 3D representations of Y, β, G and ν for $NbInS_2$ and $NbInSe_2$ are shown in Figs. 2 and 3, respectively. For isotropic substances, 3D graphs must be spherical, whereas any variation from this form indicates anisotropy.[53–55] The graphical shapes of Y, β, G and ν of $NbInS_2$ are less spherical than those of $NbInSe_2$, as seen in Figs. 2 and 3. Hence $NbInS_2$ is slightly more anisotropic than $NbInSe_2$.

To explain mechanical anisotropy, we calculated the maximum and minimum values of Y, βG, ν for $NbInX_2$ (X = S, Se) using ELATE code and are illustrated in Table 6. The numerical data shows that Y, β, G and ν of $NbInS_2$ are slightly more anisotropic than those of $NbInSe_2$.

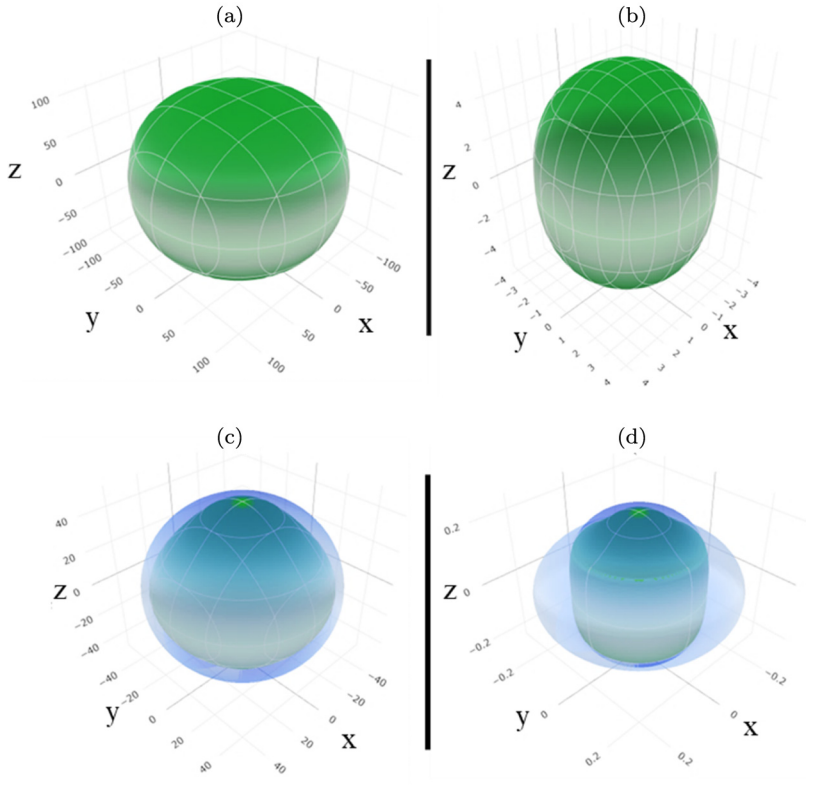

Fig. 2. (Color online) 3D representation of (a) Young's modulus, (b) compressibility, (c) shear modulus and (d) Poisson's ratio for $NbInS_2$.

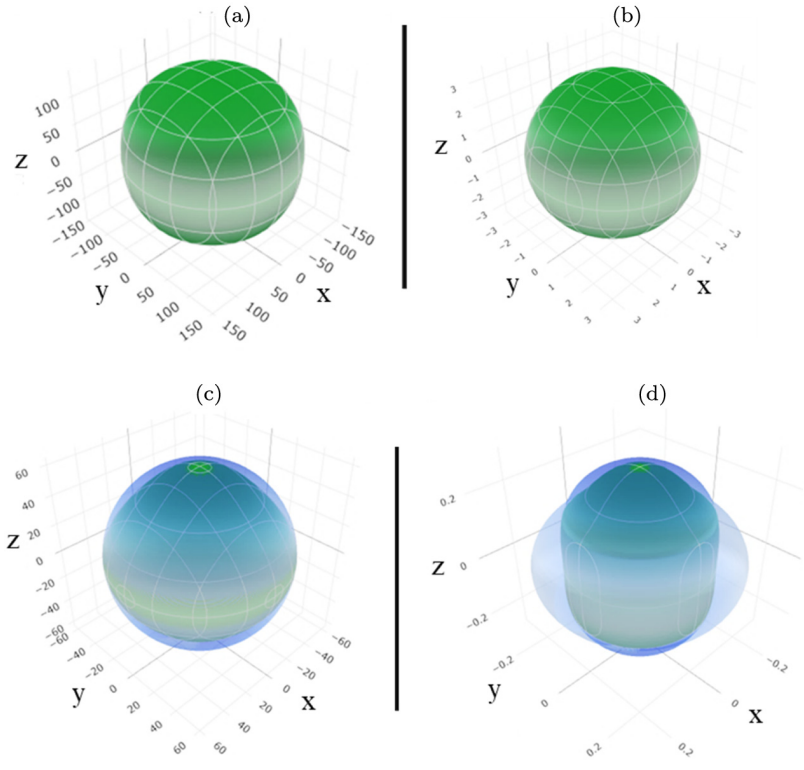

Fig. 3. (Color online) 3D representation of (a) Young's modulus, (b) compressibility, (c) shear modulus and (d) Poisson's ratio for $NbInSe_2$.

3.4. *Electronic properties*

3.4.1. *Electronic spectra and density of states*

The study of electronic band structure is essential for understanding the optical and charge transport properties of a material. The calculated band structures of $NbInX_2$ (X = S, Se) along high symmetry directions of the k-space within the first Brillouin zone at the ground state are presented in Figs. 4(a) and 4(b). It is noted that the electronic band structures of $NbInS_2$ and $NbInSe_2$ are almost identical to each other. It offers a number of significant distinctive qualities, including the type of chemical bonding and structural details. The Fermi level, E_F, is represented by the horizontal

Table 6. The minimum limit, maximum limit and anisotropy of Y (GPa), β (TPa^{-1}), G (GPa) and ν of $NbInS_2$ and $NbInSe_2$.

	Y			β			G			ν		
Species	Y_{min}	Y_{max}	A_Y	β_{min}	β_{max}	A_β	G_{min}	G_{max}	A_G	ν_{min}	ν_{max}	A_ν
$NbInS_2$	97.0	124.1	1.28	4.13	5.55	1.34	43.23	52.05	1.20	0.19	0.30	1.54
$NbInSe_2$	137.1	151.3	1.10	3.28	3.39	1.03	55.15	60.71	1.41	0.21	0.29	1.41

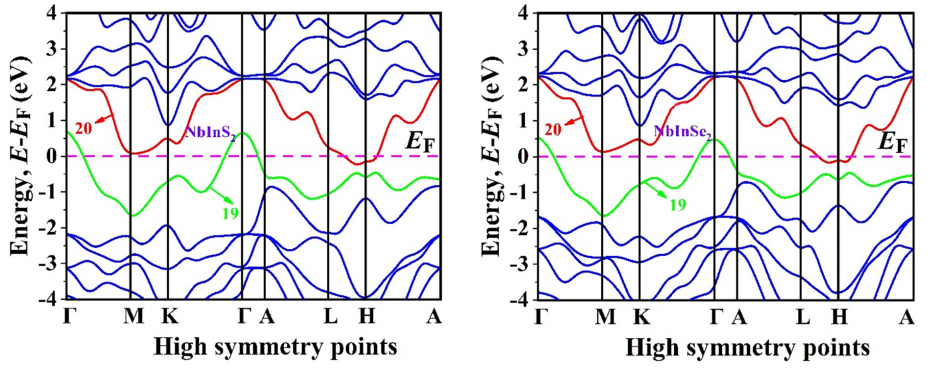

Fig. 4. (Color online) The electronic spectra of (a) $NbInS_2$ and (b) $NbInSe_2$ along high symmetry directions in the 1st Brillouin zone.

dashed line which is drawn at 0 eV. At the Fermi level, it is shown that the valence and conduction bands for both compounds overlap, preventing the appearance of a band gap. Therefore, these compounds exhibit metallic properties.

The detailed features of band structure and the bonding characteristics of these compounds can be understood from the study of the total and partial DOS, which are presented in Figs. 5(a) and 5(b). The density of states explains the number of occupied states per interval of energy at each energy level. From Fig. 5(a), it is observed that the valence bands between -4 and -2 eV are due to major contributions of S $3p$ states, which means that these orbitals are the main contributors to the electronic states within this energy range. In this case, the sulfur atoms form covalent bonds by overlapping their $3p$ orbitals with $4d$ orbitals of Nb atoms. Again, the bands extending from -2 eV to near the Fermi level mainly originate due to Nb $4d$ states. At the Fermi level, DOS arises due to the hybridized contributions from the Nb $4d$, In $5p$ and S $3p$ electronic states. In the conduction bands (extending from 1 eV to 4 eV) Nb $4d$, In $5p$ and S $3p$ states make up the majority of the total DOS. $NbInSe_2$ shows almost similar characteristics.

Both of our investigated compounds are metallic, as evidenced by their limited DOS values at the Fermi level. The total DOS at E_F for $NbInS_2$ and $NbInSe_2$ is approximately 1.34 and 1.20 states/eV unit cell, respectively. $NbInS_2$ is therefore regarded to be slightly more conductive than $NbInSe_2$.

Another crucial parameter is the pseudogap, E_P, which is the gap between the bonding and anti-bonding states. Electronic stability[56,57] of a compound can be significantly impaired if a pseudogap is present around the Fermi level of the total DOS. The bonding and anti-bonding peaks in $NbInS_2$ and $NbInSe_2$ lie within 0.50 and 0.30 eV, respectively, from the Fermi level. The electrons in the levels above E_P become delocalized at this distance from the Fermi level and the material is said to have metalized.

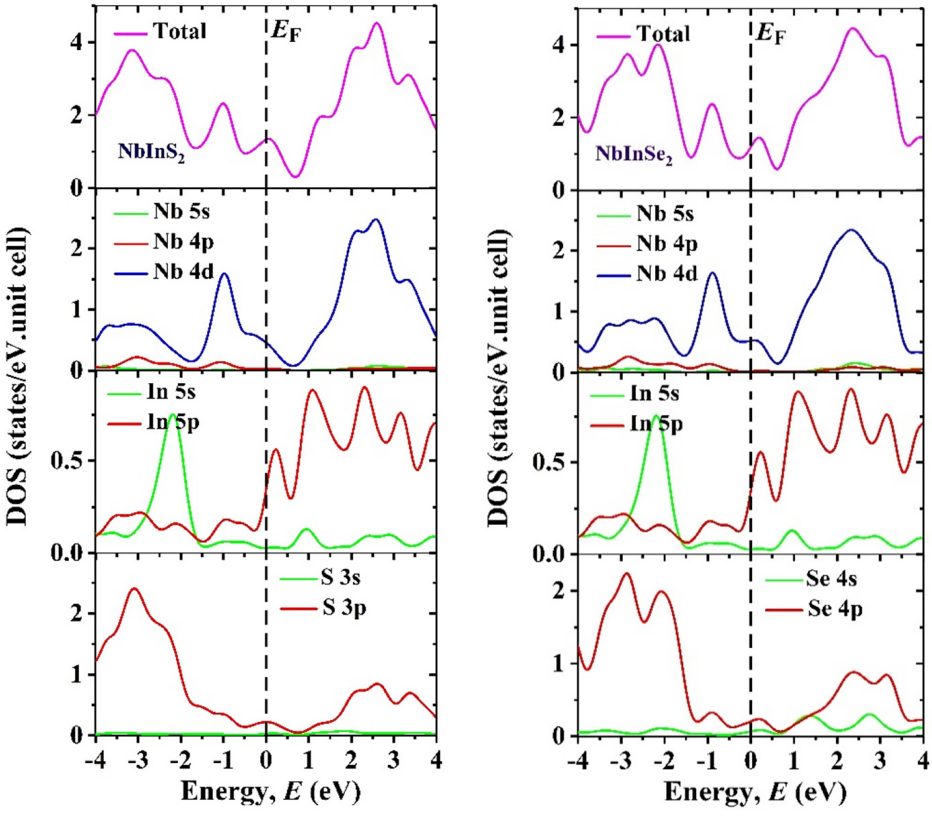

Fig. 5. (Color online) The total and projected densities of states of (a) $NbInS_2$ and (b) $NbInSe_2$.

3.4.2. *Fermi surface*

The Fermi surface is the boundary between occupied and unoccupied electron states in reciprocal space at absolute zero.[58] The Fermi surface can be used to predict thermal, optical, electrical and magnetic behavior of metals and semimetals. The Fermi surfaces of the $NbInX_2$ (X = S, Se) are shown in Fig. 6. The Fermi surface of all compounds have unique geometries that make them simple to recognize from one another. Fermi surfaces are made up of bands 19 and 20 of both compounds that cross the Fermi level. Both compounds have electron and hole-like sheets, as seen in the figures. It is to be observed that the density of states around the Fermi surface is dominated by d-states of Nb, with modest contributions from s- and p-states of S, Se and In atoms for both compounds. Due to their predominant involvement in the Fermi level, Nb-4d electrons are used to investigate the metallicity of $NbInX_2$ (X = S, Se), which can be obtained from the DOS in Fig. 5. Figure 6 shows that a hole-like sheet forms surrounding the zone center Γ-point for $NbInS_2$ for band 19. On the other hand,

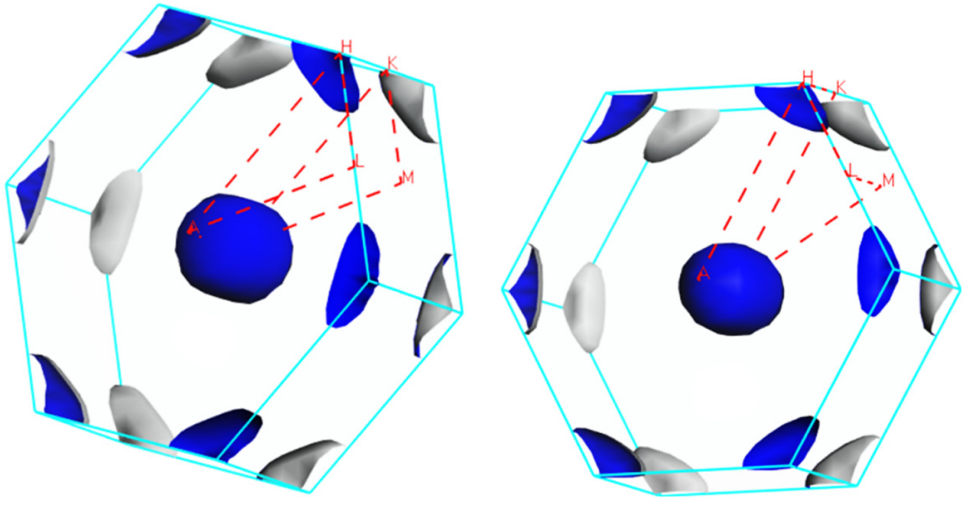

(a) (b)

Fig. 6. (Color online) Fermi surface for (a) $NbInS_2$ and (b) $NbInSe_2$, respectively.

for band 20, electron-like Fermi sheets develop around the H-point. A similar Fermi surface topology is found for $NbInSe_2$.

3.4.3. *Electron density map*

The electron density map provides us with a strong grasp of the type of bonding that exists between the crystal's atoms. Figure 7 depicts the charge density distribution

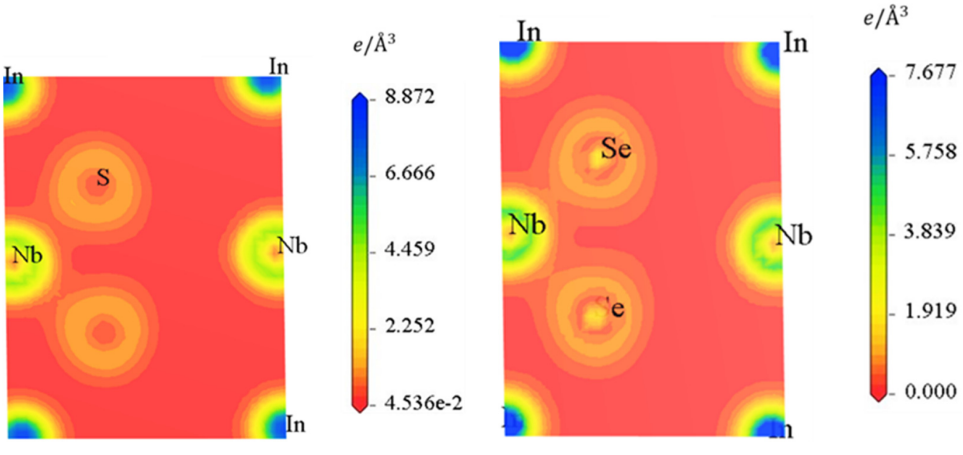

(a) (b)

Fig. 7. (Color online) Electron density distribution maps of (a) $NbInS_2$ and (b) $NbInSe_2$ in the (111) plane.

maps (e/Å^3) for NbInX_2 (X = S, Se) along (111) crystallographic plane to comprehend the distribution of the entire electronic charge in these materials. The intensity of electronic charge density is depicted by the color scales adjacent to the map in which blue color denotes high electron density, whereas red color denotes low electron density. It is possible to recognize covalent bonds by looking at the concentration of charges between two atoms. Ionic bonds may be present if there is a balance between the negative and positive charges at the atom sites.

Figures 7(a) and 7(b) make clear that strong covalent bonding exists in S–Nb and Se–Nb for $NbInS_2$ and $NbInSe_2$, respectively. In this case, Nb 4d states and S(Se) 3p (4p) states hybridized strongly. According to the Mulliken atomic population analysis, these findings are reliable. The bonding of S–Nb is slightly stronger than that of Se–Nb bond. Since the electron distributions of In and S/Se atoms do not overlap, it can be said that In–S and In–Se bonds are ionic. Furthermore, both compounds show significant metallic bonding between the Nb atoms. Hence the studied compounds are a combination of covalent, ionic and metallic bonding. The Mulliken bond population study also supports it.

3.5. *Vibrational property and dynamical stability*

A material's phonon dispersion curve (PDC) is crucial because it provides critical details on dynamical stability, phase transitions and vibrational contributions to characteristics including thermal expansion, Helmholtz-free energy and heat capacity.[59] Here we have computed the PDC and phonon density of states (PHDOS) at the ground state to access the dynamical stability of NbInX_2 (X = S, Se). Density functional perturbation theory (DFPT) and the finite displacement method (FDM) have been used for this purpose.[60,61] In Figs. 8(a) and 8(b), the PDC along the high symmetry directions of the Brillouin zone and the total as well as partial PHDOS of NbInX_2 (X = S, Se) are shown. The dynamical stability of our studied compounds is

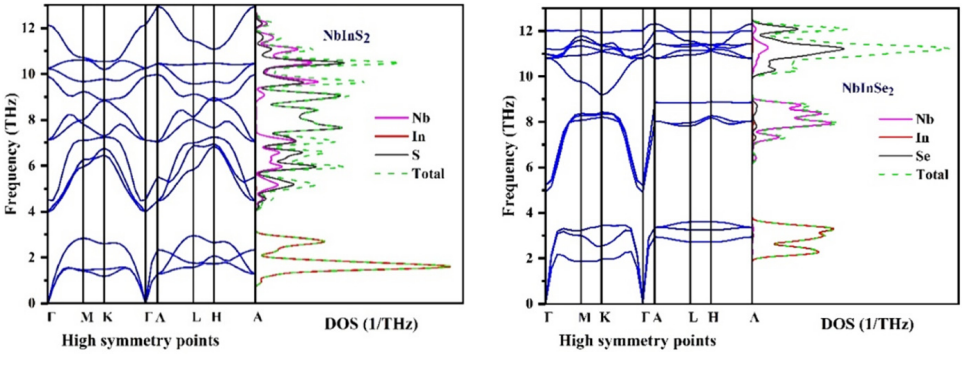

(a) (b)

Fig. 8. (Color online) The phononic spectra along with PHDOS for (a) $NbInS_2$ and (b) $NbInSe_2$.

confirmed by the presence of positive phonon frequencies throughout the entire Brillouin zone.

The phonon spectra of our investigated compounds have 12 phonon branches, comprising three acoustic modes and nine optical modes because both of the compounds contain four atoms in their unit cell. The presence of zero phonon frequency at the zone center Γ-point is another indication of dynamical stability. The optical properties of the compounds are characterized by the optical phonon modes. Figure 8 (a) shows that the lower and upper optical modes are overlapped but a noticeable band gap exists between the lower optical and acoustic modes for $NbInS_2$. Moreover, the lower and upper optical modes, as well as the acoustic and lower optical modes, are separated from one another by phonon band gap in $NbInSe_2$.

The partial PHDOS of Fig. 8(a) depicts that the acoustic modes originating from the coherent vibration of heavier In atoms. The lower and upper branches of optical modes arise due to the vibration of Nb and S atoms. Figure 8(a) also shows that S atom is only responsible for the phonon frequency from 7.5 THz to 9.4 THz. Again, the acoustic, lower and upper optical modes of $NbInSe_2$ are mainly originate due to the vibration of heavier In, Nb and lighter Se atom, respectively. Peaks in the PHDOS are created by the flatness of the bands, and their uphill and downward slope diminishes the heights of these peaks overall. From Fig. 8(b), it is observed that the acoustic branches are linear near the Γ-point, and the slope of these modes is given by a combination of the crystal's elastic constants.

3.6. *Bond population analysis*

The analysis of the Mulliken bond population is important to understand the electron density distribution among different bonds. By using the bond overlap population (BOP) technique, bonding and anti-bonding strengths are measured.[62] The BOP is interpreted as follows: A material's bonding can be expressed in one of three ways: (i) zero (no significant interaction between the electronic populations of the two atoms), (ii) positively (the neighbor atoms are bound), (iii) negatively (the atoms are anti-bonded).[62] The higher values of BOP indicate a higher level of covalency in a compound. The level of covalency of the bonds is expressed as S–Nb > Se–Nb. On the other hand, the order of the ionicity level is found in chemical bonds by reversing of this order. Hence Se–Nb bond is more ionic than S–Nb bond.

In the Mulliken population analysis, the charge spilling parameter represents the amount of missing valence charge in the projection. A small spilling parameter implies a good projection of the electronic bonds. According to the spilling parameters for $NbInS_2$ and $NbInSe_2$, only around 0.36% and 0.22% of the valence charge were missing in the projection, respectively.

Table 7 shows that for both compounds, the electronic charge is transferred from Nb and In to the S/Se atom. This leads us to the conclusion that $NbInX_2$ ($X = S, Se$) contains ionic bonds between its atoms.

Table 7. Charge spilling (%), Mulliken atomic population and effective valence charge (EVC) of $NbInS_2$ and $NbInSe_2$.

Compound	Atom	Charge spilling	Mulliken atomic population					EVC
			s	*p*	*d*	Total	Charge	
$NbInS_2$	Nb	0.36%	2.37	6.53	4.16	13.07	0.23	+3.77
	In		1.49	1.19	9.99	12.67	0.33	+2.67
	S		1.79	4.34	0.00	6.13	−0.13	+1.87
$NbInSe_2$	Nb	0.22%	2.53	6.76	4.13	13.43	0.18	+3.82
	In		1.92	1.15	9.99	13.43	0.12	+2.88
	Se		1.53	4.23	0.00	5.76	−0.15	+1.85

The effective valence charge (EVC), which is the distinction between the formal ionic charge and the Mulliken charge on the anion species in the crystal, can be used to calculate the covalent or ionic bonding strength with respect to the level of covalency or ionicity.[63,64] In an ideal ionic bond, the value of EVC is zero whereas a nonzero value denotes the degree of covalency. The strength of a covalent bond is increased by increasing positive values that are greater than zero. Hence, there is significant covalency in chemical bonding inside the $NbInX_2$ (X = S, Se).

3.7. *Calculations of Vickers hardness*

To explain the bonding characteristics and assess the intrinsic and extrinsic properties of $NbInX_2$ (X = S, Se), the Vickers hardness can be calculated. In this study, we used a formulated equation by Gao[65] to calculate the Vickers hardness of our studied compounds using Mulliken bond population analysis within the first-principles method. Due to the delocalization of metallic bonding, there is no significant correlation between hardness and metallic bonding.[66] Gao *et al.*[67] corrected this equation to incorporate compounds with partial metallic bonds as a result of delocalized metallic bonding and expressed as follows:

$$H_v^{\mu} = 740(P^{\mu} - P^{\mu'})(\nu_b^{\mu})^{-\frac{5}{3}}, \tag{29}$$

where P^{μ} is the Mulliken bond overlap population of the μ-type bond, $P^{\mu'} = n_{\text{free}}/V$ is the metallic population, V is unit cell volume, $n_{\text{free}} = \int_{E_P}^{E_F} N(E)dE$ is the number of free electrons in a unit cell, v_b^{μ} is the volume of μ-type bond, which is determined by the bond length d^{μ}. The number of bonds N_b^{μ} of μ-type per unit volume can be written as $v_b^{\mu} = (d^{\mu})^3/\sum_v[(d^{\mu})^3 N_b^{\mu}]$. For a complex multiband crystal, the geometric average of the hardness of all bonds can be written as[67,68]

$$H_v = \left[\prod^{\mu} (H_v^{\mu})^{n^{\mu}}\right]^{1/\sum n^{\mu}}, \tag{30}$$

where n^{μ} denotes the number of μ-type bonds. The calculated Vickers hardness with relevant quantities for $NbInX_2$ (X = S, Se) are listed in Table 8 for the first time. The

Table 8. Calculated Mulliken bond overlap population P^{μ} with bond number N^{μ}, bond length d^{μ} (Å), metallic population $P^{\mu'}$, volume of μ-type bond v_b^{μ} (Å^3), bond hardness H_v^{μ} (GPa) and Vickers hardness H_v (GPa) of $NbInS_2$ and $NbInSe_2$.

Compound	Bond	N^{μ}	P^{μ}	d^{μ}	$P^{\mu'}$	v_b^{μ}	H_v^{μ}	H_{ν}	Level of covalency (%)
$NbInS_2$	S–Nb	2	1.12	2.4107	0.0073	37.53	1.96	1.96	Highest (100)
$NbInSe_2$	Se–Nb	2	0.69	2.5763	0.0041	39.35	1.12	1.12	Lowest (62)

estimated values of Vickers hardness of $NbInS_2$ and $NbInSe_2$ are 1.96 and 1.12 GPa, respectively. Thus, softness and ease of machining are expected for $NbInX_2$ (X = S, Se).

The bonding metallicity[67,69] of a material can be evaluated with $f_m = P^{\mu'}/P^{\mu}$. The calculated values for S–Nb and Se–Nb are 0.0065 and 0.0059, respectively. Hence, the degree of metallicity of S–Nb and Se–Nb bond is almost same.

3.8. *Optical properties*

The optical properties of a material explain its interaction with the incident light. The study of these characteristics at visible light is especially important for photovoltaic applications. Here we have studied various energy-dependent optical parameters such as dielectric constant $\varepsilon(\omega)$, absorption coefficient $\alpha(\omega)$, optical conductivity $\sigma(\omega)$, loss function $L(\omega)$, reflectivity $R(\omega)$, the refractive index $n(\omega)$ and extinction coefficient $k(\omega)$.

The optical properties of $NbInS_2$ and $NbInSe_2$ are calculated using the frequency-dependent complex dielectric function $\varepsilon(\omega) = \varepsilon_1(\omega) + i\varepsilon_2(\omega)$ for the first time, where $\varepsilon_1(\omega)$ and $\varepsilon_2(\omega)$ are the real and imaginary parts of dielectric function. $\varepsilon_2(\omega)$ is obtained using the formula given in Refs. 70 and 71 and $\varepsilon_1(\omega)$ is derived from $\varepsilon_2(\omega)$ by the Kramers–Kronig transform.[70,71] The optical functions of $NbInX_2$(X = S, Se) are evaluated at [100] and [001] polarization directions of the electric field. The electric field polarization-dependent behavior of the optical constants provides important insights into optical and electronic anisotropy. Intra-band as well as inter-band transitions have contributed to the dielectric functions of metallic compounds. Hence, an empirical Drude term is necessary to analyze the optical parameters of the metallic system.[71,72] As our studied compounds are metallic, we have used 0.05 eV for Drude damping and 6 eV (5 eV) for the plasma frequency of $NbInS_2$ ($NbInSe_2$). The calculated optical parameters of $NbInX_2$ (X = S, Se) for photon energies up to 25 eV are displayed in Fig. 9.

(a) Dielectric constants

The dielectric function, $\varepsilon(\omega)$, completely explains the electronic reaction of a material to incoming electromagnetic wave. $\varepsilon_1(\omega)$ is related to the electrical polarization of the material whereas $\varepsilon_2(\omega)$ is related with dielectric loss and describes its absorptive behavior. Energy (frequency) dependance of ε_1 and ε_2 for $NbInX_2$ (X = S, Se) are displayed in Figs. 9(a) and 9(g) along [100] and [001] polarization directions. The

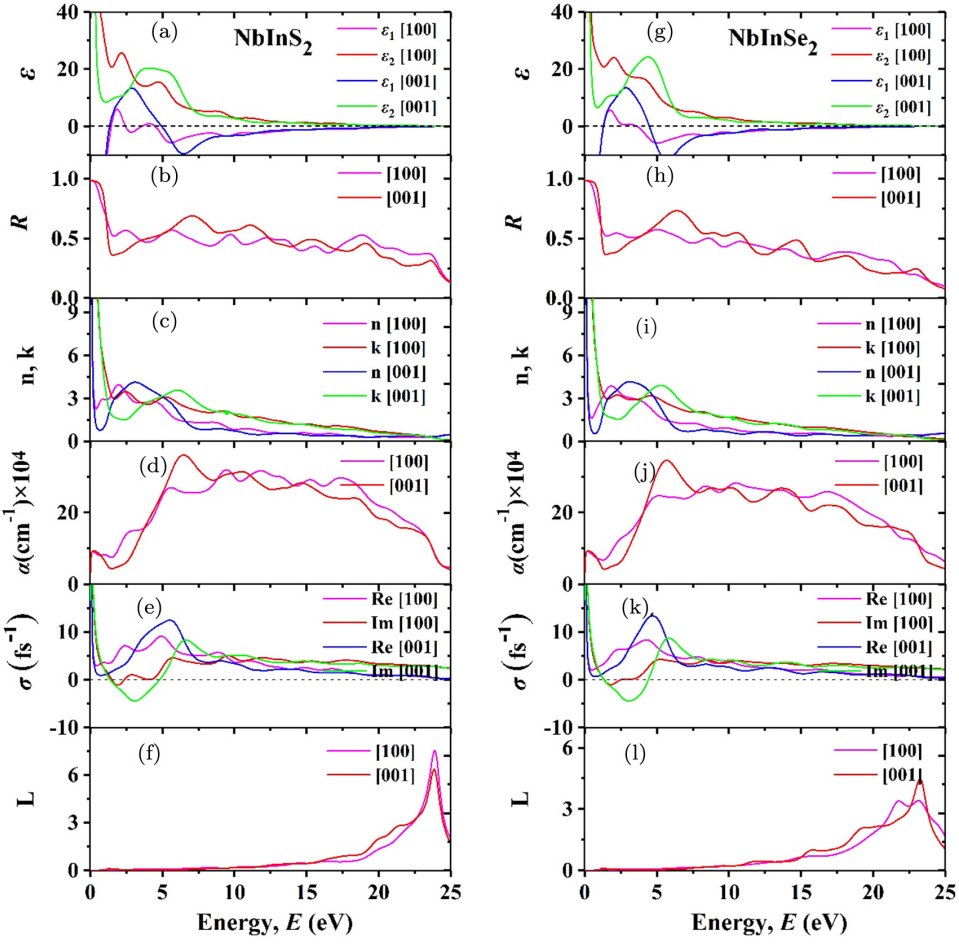

Fig. 9. (Color online) The energy-dependent (a, g) dielectric function, (b, h) reflectivity, (c, i) refractive index, (d, j) absorption coefficient, (e, k) optical conductivity and (f, l) loss function of $NbInS_2$ and $NbInSe_2$ along [100] and [001] directions.

high negative values of ε_1 suggest that both $NbInX_2$ (X = S, Se) show Drude-like behavior. For both $NbInX_2$ (X = S, Se), large value of ε_2 in the infrared and near-visible region for both polarization directions suggest high absorption of electromagnetic radiation in these regions. The figure shows that ε_1 reaches zero from below and ε_2 approaches zero from above at 23.50 and 21.83 eV for $NbInS_2$ and $NbInSe_2$, respectively. At this energy, the loss function reaches its maximum and the reflection and absorption band both abruptly decline.

(b) Reflectivity

Reflectivity is an important optical parameter that explains how much incident light is reflected from the substance. The reflectivity spectra for $NbInX_2$ (X = S, Se) compounds are shown in Figs. 9(b) and 9(h) along the polarization directions. These

figures show that both the compounds have almost similar reflectivity spectra which start with a value of ∼0.99.

Figure 9(b) demonstrates that the reflectance of $NbInS_2$ significantly drops along the [100] direction up to 1.7 eV. Thereafter, the curve exhibits nearly nonselective features up to ∼13 eV, and the reflectance is greater than 50% in this area. On the other hand, along [001] direction, the reflectivity of $NbInS_2$ gradually increases from ∼1.6 eV to ∼7 eV and then slowly decreases. Reflectivity increases from ∼35% to ∼70% in this region. $NbInSe_2$ exhibits almost similar characteristics. $NbInSe_2$ shows nearly nonselective characteristics up to ∼8 eV along [100] direction and the reflectivity is above 50%. For [001], the reflectance of $NbInSe_2$ decreases up to ∼1.5 eV, after this, the curve slightly increases and reaches a maximum value at ∼6.4 eV. We observe that $R(\omega)$ for $NbInX_2$ (X = S, Se) in [001] direction is always higher than in [100] direction. It is generally known that a material can reduce solar heating if its reflectance is ∼44% in the visible region.[73] $NbInS_2$ and $NbInSe_2$ are thus viable contenders for coating materials to lessen solar heating.

(c) Index of refraction

A detailed understanding of a material's index of refraction is essential for the correct design of optoelectronic devices. The real and imaginary parts of the refractive index of $NbInS_2$ and $NbInSe_2$ phases are shown in Figs. 9(c) and 9(i). The electromagnetic wave phase velocity in a material can be characterized by the real part of the refractive index, $n(\omega)$. The imaginary component, on the other hand, measures the absorption loss of electromagnetic radiation when it travels through a medium, which is also known as the extinction coefficient, $k(\omega)$. For both the studied compounds, $n(\omega)$ has high value at low photon energies. The static refractive index, $n(0)$, for $NbInS_2$ ($NbInSe_2$) is ∼42 (∼38) in both polarization orientations. These materials can be utilized to enhance the visual quality of electronic displays like LCD, quantum dot TVs, etc. due to the high value of $n(0)$. The extinction coefficient, $k(\omega)$, sharply decreases from its maximum value and turns to zero at about 28.7 eV for both compounds. The way that n and k change with incident photon energy for both compounds is almost identical.

(d) Absorption coefficient

The absorption coefficient measures how far light can go through a substance before it is absorbed and represents the reduction of light intensity as it passes through a substance. This measurement varies for different wavelengths of light and different materials. The absorption spectra of $NbInS_2$ and $NbInSe_2$ are presented in Figs. 9(d) and 9(j). These results clearly show that the absorption coefficients of both compounds start from zero photon energy, which is a sign of metallic nature and is consistent with the electronic band structures. For $NbInS_2$, the highest value of $\alpha(\omega)$ is almost $36 \times 10^4\,cm^{-1}$ (along [001]) at ∼6.5 eV and is $\sim 27 \times 10^4\,cm^{-1}$ (along [100]) at ∼5.6 eV. On the other hand, the highest $\alpha(\omega)$ for $NbInSe_2$ is $\sim 28 \times 10^4\,cm^{-1}$ (along [100]) at ∼10.5 eV and is $\sim 35 \times 10^4\,cm^{-1}$ (along [001]) at ∼5.7 eV. Hence, both the compounds show highest absorption in the ultraviolet region and can be

used as coating materials to protect systems that are vulnerable to photo-disintegration or photo-oxidation caused by ultraviolet light. Again, in the visible region, the highest value of $\alpha(\omega)$ for $NbInS_2$ is $\sim 15 \times 10^4\,cm^{-1}$ (along [100]) and for $NbInSe_2$ is $\sim 14.5 \times 10^4\,cm^{-1}$ (along [100]). The absorption coefficients of our studied compounds are almost comparable to that of MAX phase compounds Hf_2SC ($25 \times 10^4\,cm^{-1}$ at $\sim$12 eV),[74] anti-perovskite compounds Sc_3InB (20×10^4 cm^{-1} at $\sim$5 eV),[75] semiconductor GaAs ($(14–22) \times 10^4\,cm^{-1}$ at $\sim$4.8 eV)[76] but smaller than that of Ba_3SbN and Ba_3BiN ($12 \times 10^5\,cm^{-1}$ at $\sim$8 eV),[77] BaAgP ($6.4 \times 10^5\,cm^{-1}$ in the visible region)[78] and silicon ($18 \times 10^5\,cm^{-1}$).[79]

(e) Optical conductivity

The optical conductivity, $\sigma(\omega)$, implies optical and electrical phenomena that indicates a material have more electrical conduction under the absorption of electromagnetic radiation.[80] According to the Figs. 9(e) and 9(k), $\sigma(0)$ has a finite value which indicates that the materials have no energy band gap, as evident from band structure. Therefore, optical conductivities and hence electrical conductivities of a material increase with absorbing photons. The imaginary part of the conductivity becomes zero at 1.47 ($NbInS_2$) and 1.35 eV ($NbInSe_2$) of photon energy. The highest value of the real part of optical conductivity of $NbInS_2$ ($NbInSe_2$) in the visible range is $7\,fs^{-1}$ ($6\,fs^{-1}$) along [100] and $6\,fs^{-1}$ ($6.6\,fs^{-1}$) along [001]. However, the highest optical conductivity for $NbInS_2$ ($NbInSe_2$) is $12.6\,fs^{-1}$ ($13.4\,fs^{-1}$) in the ultraviolet region.

(f) Loss function

The loss function, $L(\omega)$, is a fundamental parameter, which explains how much energy is lost when a fast electron passes through a substance.[80] The loss function, $L(\omega)$, of $NbInX_2$ (X = S, Se) is depicted in Figs. 9(f) and 9(l). The largest peak in $L(\omega)$ shows plasma resonance caused by collective movements of charge excitations at a particular frequency, referred to as plasma frequency ω_P. Plasma frequency of a material is induced when $\varepsilon_1(\omega)$ reaches zero from below and $\varepsilon_2(\omega)$ is very small at such energy. The plasma frequencies of $NbInS_2$ and $NbInSe_2$ are 24 and 23 eV, respectively, for both polarization directions. This suggests that the studied compounds are predicted to be transparent when the frequency of incoming light is greater than $\sim$24 eV ($\sim$23 eV) for $NbInS_2$ ($NbInSe_2$), and the optical properties will exhibit insulating behavior.

3.9. *Acoustic velocities and their anisotropy*

Acoustics is a discipline of physics that studies the creation, transmission, and consequences of sound. Sound velocities in elastically anisotropic substances depend on the directions of propagation of elastic waves.

In a polycrystalline material, the average sound velocity v_a is estimated, using the transverse and longitudinal sound velocities[81]:

$$v_a = \left[\frac{1}{3}\left(\frac{2}{v_t^3} + \frac{1}{v_l^3}\right)\right]^{-1/3}, \tag{31}$$

where v_l and v_t are the respective longitudinal and transverse sound velocities that are derived from Navier's equation[81] as follows:

$$v_l = \left(\frac{3B + 4G}{3\rho}\right)^{1/2} \quad \text{and} \quad v_t = \left(\frac{G}{\rho}\right)^{1/2}. \tag{32}$$

One of the most important factors, which determines whether a sound wave will be reflected or transmitted through a material is its acoustic impedance, or Z. If the differences in Z values between the two substances are considerable near the border, the reflection will be large. On the other side, there will not be any reflection (or refraction) if the impedances are equivalent. The acoustic performance of the instrument might be estimated from acoustic impedance. It also has a large influence on the sound produced. There are many uses of acoustic impedance, such as in the development of transducers, acoustic sensors, noise reduction in aviation engines, factories, transportation, and different submersible acoustic devices. The acoustic impedance of $NbInX_2$ (X = S, Se) may be computed using the following equation[28]:

$$Z = \sqrt{\rho G}, \tag{33}$$

where G and ρ are the shear modulus and density of the material, respectively. It is noticeable that a material's acoustic impedance will be high if its density and shear modulus are both high.

Sound intensity measurement is an effective approach for measuring the flow of sound energy as a time-averaged vector quantity. Various configurations of sound boards are designed by the intensity of sound radiation. The sound intensity, I, is defined with shear modulus and density as[28,82]

$$I \approx \sqrt{G/\rho^3}, \tag{34}$$

where $\sqrt{G/\rho^3}$ is known as the radiation factor and is typically used to choose materials for sound board construction. Table 9 demonstrates the estimated values of sound velocities, acoustic impedance and radiation factor for $NbInS_2$ and $NbInSe_2$.

Since our investigated compounds are anisotropic crystal, the sound velocities of $NbInS_2$ and $NbInSe_2$ can be determined with pure transverse and longitudinal modes from the symmetry of the crystal and propagation of crystallographic direction. The acoustic velocities along [100] and [001] directions for hexagonal crystal are

Table 9. Density ρ (g/cm^3), transverse, longitudinal and average sound velocities v_l, ν_t, ν_a (ms^{-1}), acoustic impedance Z (Rayl) and sound intensity, I (m^4/kg.s) of $NbInS_2$ and $NbInSe_2$.

Compounds	ρ	ν_t	ν_l	ν_a	$Z(\times 10^6)$	I
$NbInS_2$	5.30	3009.42	5078.63	3333.13	15.95	0.568
$NbInSe_2$	6.22	3085.07	5354.53	3425.63	19.19	0.496

given by[83]

$$[100] : [100]v_l = \sqrt{\frac{C_{11} - C_{12}}{2\rho}}, \quad [010]v_{t1} = \sqrt{\frac{C_{11}}{\rho}}, \quad [001]v_{t2} = \sqrt{\frac{C_{44}}{\rho}}, \tag{35}$$

$$[001] : [001]v_l = \sqrt{\frac{C_{33}}{\rho}}, \quad [100]v_{t1} = [010]v_{t2} = \sqrt{\frac{C_{44}}{\rho}}, \tag{36}$$

where v_{t1} and v_{t2} are the 1st and 2nd transverse modes, respectively. Direction-dependent sound velocities of $NbInS_2$ and $NbInSe_2$ are represented in Table 10.

It is worth noting that substantial anisotropy is evident in $NbInS_2$ and $NbInSe_2$.

3.10. *Thermophysical properties*

3.10.1. *Grüneisen parameter*

The Grüneisen parameter, γ, is a dimensionless parameter that contributes a helpful link with expansion coefficient, bulk modulus, density and specific heat. The Grüneisen parameter can provide a beautiful description of anharmonic effects in a solid. Moreover, the low values of γ within the compounds show low anharmonic effects. The Grüneisen parameter of $NbInS_2$ and $NbInSe_2$ is calculated using the following expression[84]:

$$\gamma = \frac{3(1+v)}{2(2-3v)}. \tag{37}$$

The calculated values of γ of $NbInS_2$ and $NbInSe_2$ are 1.41 and 1.50, respectively. The value of the Grüneisen parameter for different metals are given in Refs. 85 and 86. For materials with Poisson's ratios between 0.05 and 0.46, γ ranges from 0.85 to 3.5387.[86] Our estimated values of γ for $NbInS_2$ and $NbInSe_2$ (shown in Table 11) are within this range.

3.10.2. *Debye temperature*

Debye temperature (Θ_D) is a characteristic temperature of crystals which determine the thermodynamic properties of materials. It links several physical parameters of materials such as melting point, specific heat and thermal conductivity.

Table 10. Sound velocities (ms^{-1}) of $NbInS_2$ and $NbInSe_2$ along different propagation directions.

Propagation directions		$NbInS_2$	$NbInSe_2$
[100]	$[100]v_l$	3135.31	3121.08
	$[010]v_{t1}$	5221.51	5335.08
	$[001]v_{t2}$	3006.28	3124.17
[001]	$[001]v_l$	4692.43	5262.71
	$[100]v_{t1}$	3006.28	3124.17
	$[010]v_{t2}$	3006.28	3124.17

The Debye temperature is determined by the following equation[87]:

$$\Theta_D = \frac{h}{k_B}\left(\frac{3n}{4\pi V_o}\right)^{\frac{1}{3}} v_a, \tag{38}$$

where h is Planck's constant, k_B is Boltzmann's constant, V_o is the optimized volume, and n is the number of atoms in the unit cell. When the temperature T is greater than Θ_D, all the modes of vibration possess energy $\sim k_B T$. In other words, when T is less than Θ_D,[88] the more frequent modes are regarded as frozen. Θ_D measures the covalent bonding strength of a crystal. In this study, our estimated value of Θ_D for $NbInS_2$ ($NbInSe_2$) is 361 K (378 K) (shown in Table 11). It is observed that the strength of covalent bond in $NbInS_2$ is slightly smaller than that of $NbInSe_2$. Moreover, Θ_D is closely linked with e–ph (electron–phonon) coupling parameter as well as superconducting transition temperature. It is well known that a substance's phonon thermal conductivity decreases with decreasing Θ_D. Therefore, $NbInS_2$ is thermally low conductive and treating as a thermal barrier coating (TBC) material.

3.10.3. *Melting temperature*

A material's melting point provides crucial information about its bonding strength as well as its thermal expansion coefficient. Materials with a high melting temperature, T_m, possess small thermal expansion and significant bonding energy.[28] T_m for $NbInS_2$ and $NbInSe_2$ is estimated using following empirical equation[89]:

$$T_m = 354\,\text{K} + (4.5\,\text{K/GPa})\left(\frac{2C_{11} + C_{33}}{3}\right) \pm 300\,\text{K}. \tag{39}$$

Our estimated values of T_m for $NbInS_2$ and $NbInSe_2$ are 963 and 1144 K, respectively (from Table 11). The uncertainty in the calculation of T_m is ±300 K for both compounds. As a result, compared to $NbInS_2$, $NbInSe_2$ is a better choice for high-temperature applications.

3.10.4. *Thermal expansion coefficient*

The thermal expansion coefficient, α, of crystalline materials may be used to understand how materials respond under different thermodynamical constraints, such as specific heat, thermal conductivity, the energy band gap, and electron effective mass of crystal owing to temperature variation. In this study, α of $NbInS_2$ and $NbInSe_2$ is calculated using the following equation[28,82]:

$$\alpha = (1.6 \times 10^{-3})G^{-1}, \tag{40}$$

where G is referred as isothermal shear modulus. α of solids is also correlated with melting temperature: $\alpha \approx 0.02/T_m$.[82] The values of α for $NbInS_2$ and $NbInSe_2$ are presented in Table 11.

The most useful measurement of a material is its heat capacity because it is closely related to its thermodynamical characteristics. Heat capacity also has impacts on the

Table 11. The Debye temperature Θ_D (K), thermal expansion coefficient α (K^{-1}), wavelength of the dominant phonon mode λ_{dom} (m) at room temperature, melting temperature T_m (K), heat capacity per unit volume ρC_P (J/m^3K) and Grüneisen parameter γ of $NbInS_2$ and $NbInSe_2$.

Species	Θ_D	T_m	α ($\times 10^{-5}$)	λ_{dom} ($\times 10^{-12}$)	ρC_P ($\times 10^5$)	γ
$NbInS_2$	361	963	3.33	139.0	4.95	1.41
$NbInSe_2$	378	1144	2.70	143.4	5.26	1.50

mechanical, electrical and optical properties of solids. The expression of total thermal energy per unit volume of a material is $3k_BT/\Omega$, where Ω is the volume of an atom, and $N = 1/\Omega$ is the number of atoms per unit volume. The change in thermal energy per unit change in temperature is referred to as a material's heat capacity per unit volume, ρC_P, giving[28,82]

$$\rho C_P = \frac{3k_B}{\Omega}. \tag{41}$$

Knowing a material's heat capacity also gives us a better understanding of its thermal conductivity and thermal diffusivity. It is well understood that increased heat capacity results in better thermal conductivity and lower thermal diffusivity. As the temperature rises, so does the heat capacity.

The wavelength at which the apex of the phonon distribution curve occurs is known as the phonon's dominant wavelength, λ_{dom} (m). It is calculated using the acoustic velocity. λ_{dom} for $NbInS_2$ and $NbInSe_2$ at room temperature has been computed using the following expression[90,91]:

$$\lambda_{\text{dom}} = \frac{12.566 v_a}{T} \times 10^{-12} \approx \frac{1}{T}\sqrt{\frac{Y}{\rho}} \times 10^{-11}. \tag{42}$$

From the equation, it is noted that if a material has a higher average sound velocity, the dominant phonon will have a longer wavelength. Table 11 demonstrates that $NbInSe_2$ has a dominating phonon with a longer wavelength than $NbInS_2$.

3.10.5. *Anisotropy of minimum thermal conductivity*

Minimal thermal conductivity, k_{min}, is the lowest attainable amount of intrinsic thermal conductivity of a material at high temperatures. The mean interatomic distance and the mean free path of phonons are almost identical in this instance. k_{min} of a compound can be calculated using the Clarke's model[90]:

$$k_{\text{min}} = k_B v_a (V_{\text{atomic}})^{-2/3}, \tag{43}$$

where V_{atomic} is the average volume per atom. The calculated values of k_{min} for both the compounds are shown in Table 12. It is known that the ideal value of minimal thermal conductivity[92] is $1.25\,W\,m^{-1}\,K^{-1}$ which is employed in the selection of suitable thermal barrier coating (TBC) materials. Our estimated k_{min} values for both

Table 12. The number of atoms per mole n (m^{-3}) and direction-dependent minimum thermal conductivity (W/m.K) of $NbInS_2$ and $NbInSe_2$.

Compound	n (10^{28})	$[100]k_{min}^{Cahill}$	$[001]k_{min}^{Cahill}$	k_{min}^{Clarke}
$NbInS_2$	4.79	0.834	0.786	0.607
$NbInSe_2$	5.08	0.884	0.879	0.649

the titled compounds are much lesser than that of the reference value. As a result, our investigated compounds are prospective candidates for TBC materials.

A material that is elastically anisotropic also has anisotropy in their minimum thermal conductivity. The anisotropy of $k_{min}$is determined by v_l and v_t along distinct crystallographic axes. k_{min} of $NbInX_2$ (X= S, Se) along various crystallographic axes is estimated using Cahill's model[93]:

$$k_{min} = \frac{k_B}{2.48} n^{2/3}(v_l + v_{t1} + v_{t2}) \quad \text{and} \quad n = N/V, \tag{44}$$

where n is the number of atoms per unit volume, and N denotes the total number of atoms in the cell of volume V. Table 12 shows the minimum thermal conductivity of $NbInX_2$ (X= S, Se) along the [100] and [001] directions. It can be observed that the minimum thermal conductivity along [100] is higher than that of along [001] direction for both compounds.

4. Conclusions

Here, we have theoretically studied the hitherto undiscovered mechanical, electronic, Mulliken bond population, vibrational, optical and thermophysical characteristics of synthesized chalcogenides $NbInX_2$ (X= S, Se) using DFT for the first time. The reasonable agreement between our estimated structural parameters and the experimental data demonstrates the reliability of our calculations. The analysis of Born stability criteria, Poisson's and Pugh's ratios predict the mechanical stability and brittleness of the studied compounds. The chemical and dynamical stability of the compounds are also confirmed by the study of cohesive energy and phonon spectra. Both of the phases are machinable and soft. The machinability index suggests that the compounds may be utilized as dry lubricants. The degree of anisotropy of $NbInS_2$ is larger than that of $NbInSe_2$, which is evident by 3D representations of elastic moduli.

The electrical band structure and DOS provide evidence that the compounds have metallic properties. The projected DOS exposes that Nb-4d orbitals mainly contribute in total DOS at the Fermi level for both the compounds. The bonding characteristics of the compounds are comprehensively analyzed using an electron charge density distribution map and Mulliken bond population. The results show that the investigated compounds are a combination of covalent, ionic and metallic

bonds. Almost similar Fermi surfaces of both the compounds contain both hole- and electron-like sheets. The estimated values of Vickers hardness of $NbInX_2$ ($X = S, Se$) indicate that the studied compounds are soft in nature.

The optical parameters are anisotropic and display a number of intriguing characteristics. Both compounds exhibit high absorption and significant optical conductivity in the ultraviolet region. Hence $NbInX_2$ ($X = S, Se$) may be used as a good UV absorber to protect systems that are vulnerable to photo-disintegration or photo-oxidation caused by ultraviolet light. The reflectivity of the compounds is nearly nonselective throughout a large range of photon energy. It is larger than 44% for both compounds up to around 15 eV indicating that these can be employed as solar reflectors. The compounds are suitable for use in electronic display devices because of their high value of static refractive index, $n(0)$. The loss function shows that our studied compounds will become transparent if the incoming light frequency exceeds their corresponding plasma frequencies.

The low values of Debye temperature for both compounds indicate the lower phonon thermal conductivity. $NbInSe_2$ has a lower thermal expansion coefficient and a stronger bonding strength than $NbInS_2$ due to its higher melting temperature. Our estimated values of k_{min} are much smaller than that of the reference value, which indicates that these compounds are potential candidates for thermal barrier coating material.

We expect that our work will serve as a benchmark for future research on the aforementioned characteristics of $NbInX_2$ ($X = S, Se$), since neither theoretical nor experimental studies of these characteristics have yet been conducted. We also hope that it will motivate researchers to further explore the experimental characteristics of the studied compounds.

ORCID

M. H. Mia https://orcid.org/0009-0001-2762-9058
F. Parvin https://orcid.org/0000-0002-1506-5937
A. K. M. A. Islam https://orcid.org/0000-0002-9425-5519
Mst. A. Khatun https://orcid.org/0009-0004-4019-8127

References

1. R. Eppinga and G. A. Wiegers, *Physica B* **99**, 121 (1980).
2. C. S. Sunandana, K. Chandrasekaran, G. Aravamudan and G. V. Subba Rao, *J. Less-Common Metals* **84**, 115 (1982).
3. H. Zhang, G. Chen, X. He and J. Xu, *Mater. Res. Bull.* **47**, 4483 (2012).
4. M. S. Yaseen, G. Murtaza and G. Murtaza, *Int. J. Mod. Phys. B* **34**, 2050133 (2020).
5. M. M. Hossain, M. A. Hossain, S. A. Moon, M. A. Ali, M. M. Uddin, S. H. Naqib, A. K. M. A. Islam, M. Nagao, S. Watauchi and I. Tanaka, *J. Mater. Sci. Mater. Electron.* **32**, 3878 (2021).
6. D. Wu, J. Duan, C. Zhang, K. Guo and H. Zhu, *J. Phys. Chem. C* **117**, 9121 (2013).

7. A. Soni, V. Gupta, C. M. Arora, A. Dashora and B. L. Ahuja, *Solar Energy* **84**, 1481 (2010).
8. D. Wang, W. Zheng, C. Hao, Q. Peng and Y. Li, *Chem. Commun.* **22**, 2556 (2008).
9. B. Yuan, X. Cai, X. Fang, D. Wang, R. Zhu, S. Cao, M. Wu and Q. Zhu, *Solid State Sci.* **109**, 106408 (2020).
10. M. C. Payne, M. P. Teter, D. C. Allan, T. A. Arias and J. D. Joannopoulos, *Rev. Mod. Phys.* **64**, 1045 (1992).
11. S. J. Clark, M. D. Segall, C. J. Pickard, P. J. Hasnip, M. I. J. Probert, K. Refson and M. C. Payne, *Z. Kristallogr.* **220**, 567 (2005).
12. D. Vanderbilt, *Phys. Rev. B* **41**, 7892 (1990).
13. D. M. Ceperley and B. J. Alder, *Phys. Rev. Lett.* **45**, 566 (1980).
14. J. P. Perdew and A. Zunger, *Phys. Rev. B: Condens. Matter Mater. Phys.* **23**, 5048 (1981).
15. J. Ji, K. Wang, S. Zhu and W. Zhu, *Cryst. Eng. Commun.* **23**, 2455 (2021).
16. T. H. Fischer and J. Almlof, *J. Phys. Chem.* **96**, 9768 (1992).
17. P. Wisesa, K. A. McGill and T. Mueller, *Phys. Rev. B* **93**, 155109 (2016).
18. Z. T. Y. Liu, D. Gall and S. V. Khare, *Phys. Rev. B* **90**, 134102 (2014).
19. R. Gaillac, P. Pullumbi and F. X. Coudert, *J. Phys. Condens. Matter* **28**, 275201 (2016).
20. Z. T. Y. Liu, X. Zhou, S. V. Khare and D. Gall, *J. Phys. Condens. Matter* **26**, 025404 (2014).
21. L. Fast, J. M. Wills, B. Johansson and O. Eriksson, *Phys. Rev. B* **51**, 17431 (1995).
22. S. Q. Wang and H. Ye, *J. Phys. Condens. Matter* **15**, 5307 (2003).
23. C. Kittel, *Introduction to Solid State Physics*, 5th edn. (John Wiley, 1976).
24. F. Mouhat and F. X. Coudert, *Phys. Rev. B* **90**, 224104 (2014).
25. J. Gao, Q-J. Liu and B. Tang, *J. Appl. Phys.* **133**, 135901 (2023).
26. N. I. Medvedeva, A. N. Enyashin and A. L. Ivanovskii, *J. Struct. Chem.* **52**, 785 (2011).
27. L. Kleinman, *Phys. Rev.* **128**, 2614 (1962).
28. M. I. Naher and S. H. Naqib, *Sci. Rep.* **11**, 5592 (2021).
29. J. Pokluda, M. Černý, M. Šob and Y. Umeno, *Prog. Mater. Sci.* **73**, 127 (2015).
30. J. P. Watt and L. Peselnick, *J. Appl. Phys.* **51**, 1525 (1980).
31. R. Hill, *Proc. Phys. Soc. Sec. A* **65**, 349 (1952).
32. A. Gueddouh, B. Bachir and I. K. Lefkaier, *J. Magn. Magn. Mater.* **406**, 192 (2016).
33. M. Nuruzzaman, M. A. Alam, M. A. H. Shah, F. Parvin and M. A. K. Zilani, *Comput. Condens. Matter* **12**, 1 (2017).
34. M. A. Alam, M. Nuruzzaman, M. A. H. Shah, F. Parvin and M. A. K. Zilani, *Chin. J. Phys.* **55**, 2540 (2017).
35. M. A. Hadi, N. Kelaidis, S. H. Naqib, A. Chroneos and A. K. M. A. Islam, *J. Phys. Chem. Solids* **129**, 162 (2019).
36. P. Ravindran, L. Fast, P. A. Korzhavyi, B. Johansson, J. Wills and O. Eriksson, *J. Appl. Phys.* **84**, 4892 (1998).
37. G. N. Greaves, A. L. Greer, R. S. Lakes and T. Rouxel, *Nat. Mater.* **10**, 823 (2011).
38. O. L. Anderson and H. H. Demarest, *J. Geophys. Res.* **76**, 1349 (1971).
39. A. M. M. Tanveer Karim, M. A. Hadi, M. A. Alam, F. Parvin, S. H. Naqib and A. K. M. A. Islam, *J. Phys. Chem. Solids* **117**, 139 (2018).
40. A. Savin, D. C. H. Flad, J. Flad, H. Preuss and H. G. Schnering, *Angew. Chem. Int. Ed. Engl.* **31**, 185 (1992).
41. M. A. Hadi, M. T. Nasir, M. Roknuzzaman, M. A. Rayhan, S. H. Naqib and A. K. M. A. Islam, *Phys. Status Solidi (b)* **253**, 2020 (2016).
42. S. F. Pugh, *Philos. Mag.* **45**, 823 (1954).
43. Z. Sun, D. Music, R. Ahuja and J. M. Schneider, *Phys. Rev. B* **71**, 193402 (2005).

44. L. Vitos, P. A. Korzhavyi and B. Johansson, *Nat. Mater.* **2**, 25 (2003).
45. K. J. Puttlitz and K. A. Stalter, *Handbook of Lead-Free Solder Technology for Microelectronic Assemblies*, Vol. 98 (CRC Press, New York, 2004).
46. M. J. Phasha, P. E. Ngoepe, H. R. Chauke, D. G. Pettifor and D. Nguyen-Mann, *Intermetallics* **18**, 2083 (2010).
47. X. Gao, Y. Jiang, R. Zhou and J. Feng, *J. Alloys Compd.* **587**, 819 (2014).
48. M. A. Hadi, M. A. Alam, M. Roknuzzaman, M. T. Nasir, A. K. M. A. Islam and S. H. Naqib, *Chin. Phys. B* **24**, 117401 (2015).
49. C. M. Kube and M. de Jong, *J. Appl. Phys.* **120**, 165105 (2016).
50. V. Arsigny, P. Fillard, X. Pennec and N. Ayache, in *International Conference on Medical Image Computing and Computer-Assisted Intervention*, Heidelberg: Springer Berlin Heidelberg (2005), pp. 115–122.
51. D. H. Chung and W. R. Buessem, *J. Appl. Phys.* **38**, 2010 (1967).
52. S. I. Ranganathan and M. Ostoja-Starzewski, *Phys. Rev. Lett.* **101**, 055504 (2008).
53. W. C. Hu, Y. Liu, D. J. Li, X. Q. Zeng and C. S. Xu, *Comput. Mater. Sci.* **83**, 27 (2014).
54. Q. Fan, C. Chai, Q. Wei, P. Zhou and Y. Yang, *Mater. Des.* **132**, 539 (2017).
55. W. Zhang, C. Chai, Y. Song, Q. Fan and Y. Yang, *Materials (Basel)* **11**, 740 (2018).
56. F. Parvin and S. H. Naqib, *Results Phys.* **21**, 103848 (2021).
57. I. Galanakis and P. Mavropoulos, *J. Phys. Condens. Matter* **19**, 315213 (2007).
58. S. B. Dugdale, *Phys. Scr.* **91**, 053009 (2016).
59. Y. Yun, D. Legut and P. M. Oppeneer, *J. Nucl. Mater.* **426**, 109 (2012).
60. G. Kresse, J. Furthmüller and J. Hafner, *Europhys. Lett.* **32**, 729 (1995).
61. K. Parlinski, Z. Q. Li and Y. Kawazoe, *Phys. Rev. Lett.* **78**, 4063 (1997).
62. A. Chowdhury, M. A. Ali, M. M. Hossain, M. M. Uddin, S. H. Naqib and A. K. M. A. Islam, *Phys. Status Solidi B* **255**, 1700235 (2017).
63. M. D. Segall, R. Shah, C. J. Pickard and M. C. Payne, *Phys. Rev. B* **54**, 16317 (1996).
64. R. S. Mulliken, *J. Chem. Phys.* **23**, 1833 (1955).
65. F. Gao, *Phys. Rev. B* **73**, 132104 (2006).
66. J. H. Westbrook and H. Conrad, *The Science of Hardness Testing and Its Research Applications* (ASM, Ohio, 1973).
67. H. Gou, L. Hou, J. Zhang and F. Gao, *Appl. Phys. Lett.* **92**, 241901 (2008).
68. M. A. Hadi, *Comput. Mater. Sci.* **117**, 422 (2016).
69. M. A. Hadi, M. S. Ali, S. H. Naqib and A. K. M. A. Islam, *Int. J. Comput. Mater. Sci. Eng.* **2**, 1350007 (2013).
70. Materials Studio CASTEP manual ©Accelrys (2010), http://www.tcm.phy.cam.ac.uk/castep/documentation/WebHelp/CASTEP.html.
71. S. Li, R. Ahuja, M. W. Barsoum, P. Jena and B. Johansson, *Appl. Phys. Lett.* **92**, 221907 (2008).
72. R. Saniz, L. Ye, T. Shishidou and A. J. Freeman, *Phys. Rev. B* **74**, 014209 (2006).
73. A. L. Pisello, *Eco-Efficient Materials for Mitigating Building Cooling Needs* (Woodhead Publishing, 2015), pp. 243–268.
74. K. Akter, F. Parvin, M. A. Hadi and A. K. M. A. Islam, *Comput. Condens. Matter* **24**, e00485 (2020).
75. M. A. Hossain, M. S. Ali, F. Parvin and A. K. M. A. Islam, *Comput. Mater. Sci.* **73**, 1 (2013).
76. M. D. Sturge, *Phys. Rev.* **127**, 768 (1962).
77. E. Haque, M. T. Rahman and M. A. Hossain, arXiv:1810.12526.
78. F. Parvin, M. A. Hossain, I. Ahmed, K. Akter and A. K. M. A. Islam, *Results Phys.* **23**, 104068 (2021).
79. K. Bücher, J. Bruns and H. G. Wagemann, *Appl. Phys.* **75**, 1127 (1994).

80. L. A. DeWerd and P. R. Moran, *Med. Phys.* **5**, 23 (1978).
81. M. I. Naher and S. H. Naqib, *J. Alloys Compd.* **829**, 154509 (2020).
82. M. F. Ashby, P. J. Ferreira and D. L. Schodek, *Nanomater. Nanotechnol. Des.* **87**, 146 (2009).
83. Y. H. Duan, Y. Sun, M. J. Peng and S. G. Zhou, *J. Alloys Compd.* **595**, 14 (2014).
84. G. A. Slack, *Solid State Phys. — Adv. Res. Appl.* **34**, 71 (1979).
85. M. Hasegawat and W. H. Young, *J. Phys. F: Metal Phys.* **10**, 225 (1980).
86. V. N. Belomestnykh and E. P. Tesleva, *Tech. Phys.* **49**, 1098 (2004).
87. O. L. Anderson, *J. Phys. Chem. Solids* **24**, 909 (1963).
88. J. R. Christman, Fundamentals of solid states physics (1988), http://catalog.hathitrust.org/api/volumes/oclc/16525569.html.
89. M. Fine, L. Brown and H. Marcus, *Scr. Metall.* **18**, 951 (1984).
90. D. R. Clarke, *Surf. Coat. Technol.* **67**, 163 (2003).
91. M. I. Naher and S. H. Naqib, *Results Phys.* **28**, 104623 (2021).
92. Y. Liu, V. R. Cooper, B. Wang, H. Xiang, Q. Li and Y. Gao, *Mater. Res. Lett.* **7**, 145 (2019).
93. D. G. Cahill, S. K. Watson and R. O. Pohl, *Phys. Rev. B.* **46**, 6131 (1992).